mater.scichina.com link.springer.com

Published online 21 October 2022 | https://doi.org/10.1007/s40843-022-2209-9
Sci China Mater 2023, 66(3): 1042–1052

Metal-organic framework-derived nitrogen-doped carbon-coated hollow tubular In_2O_3/CdZnS heterojunction for efficient photocatalytic hydrogen evolution

Weijie Zhang[1], Shunshun Zhao[2], Hongjie Qin[1], Qiling Zheng[1], Penghui Zhang[1], Xiaojuan Li[1], ChuanLin Li[1], TongKai Wang[1], Na Li[1], Shouwei Zhang[1*] and Xijin Xu[1*]

ABSTRACT Using photocatalytic hydrogen evolution (PHE) technology is a powerful way to solve the energy shortage. In this study, a hexagonal hollow tubular nitrogen-doped carbon (N-C)-coated In_2O_3/CdZnS heterojunction photocatalyst was *in situ* synthesized using a simple oil bath heating method. Results show that the PHE rate of N-C/In_2O_3/CdZnS (~22.87 μmol h^{-1}) is ~2.4 times that of pristine CdZnS (~9.49 μmol h^{-1}) and ~54.5 times that of pristine In_2O_3 (~0.42 μmol h^{-1}). After four cycles, the PHE rate can still retain more than 90% of the original. Its excellent photocatalytic performance is mainly attributed to the following aspects: (1) the N-C layer acts as an electron transport bridge, which ensures the efficient electron transfer of the photocatalytic reaction; (2) the hollow tubular structure enhances the light reflection and absorption; (3) the N-C/In_2O_3/CdZnS heterostructure improves the carrier recombination and photocorrosion; (4) the large specific surface area and mesoporous structure provide a large number of reactive sites. This study provides a novel idea for designing visible-light-type heterojunction catalysts.

Keywords: hollow tubular, heterojunction, photocatalyst, nitrogen-doped carbon layer

INTRODUCTION

With the rapid development of the global economy and the high consumption of traditional fossil energy, energy crisis and environmental pollution have become imminent [1–3]. Therefore, renewable and clean energy must be utilized to comply with the global trend of green and low-carbon development. Given its high energy density (1.43×10^5 kJ kg^{-1}), rich source of raw materials, and zero carbon emissions after combustion, hydrogen energy is the best choice to replace traditional fossil energy in the future [4–8]. Photocatalytic hydrogen evolution (PHE) technology is undoubtedly one of the best choices for achieving low-cost and high-yield hydrogen production [9–13].

In recent years, metal-organic frameworks (MOFs) have been considered promising PHE materials because of their high specific surface area, abundant porous structure, and highly dispersed metal sites [14–18]. Similarly, MOF-based materials as precursors have obvious advantages in the preparation of metal sulfides, metal phosphides, metal oxides, and porous carbon materials, opening opportunities for the comprehensive application of MOFs. Shen *et al.* [19] synthesized tubular In_2S_3/In_2O_3 heterostructures with porous shells through the controlled sulfurization of MIL-68(In) and found that these heterostructures show excellent performance in the photocatalytic coupling of amines to imines. Han *et al.* [20] synthesized a rhombohedral corundum/cubic In_2O_3 junction through the simple pyrolysis of NH_2-MIL-68(In), which is not only nontoxic but also exhibits excellent PHE performance. Li *et al.* [21] obtained hollow tubular In_2O_3@C through the pyrolysis of MIL-68(In) and found that its PHE performance is comparable to that of Pt/In_2O_3. This result can be ascribed to the fact that the carbon atoms are ordered at the molecular level of the MOF precursor, and thus the In_2O_3 surface is covered with a uniform carbon layer, forming a core-shell structure in close contact. This core-shell structure and the subsequently formed hollow structure can improve the light absorption and reflection in the hollow structure, thus accelerating the photocatalytic reaction rate [19,22,23]. However, the high photogenerated electron-hole recombination rate of N-C/In_2O_3 limits its PHE rate. In addition, the formation of heterostructures promotes the separation of photogenerated carriers and increases the number of reaction sites [24,25], thereby accelerating the photocatalytic reaction.

Due to its special structure, CdZnS solid solution has a lower photogenerated carrier recombination rate and a controllable energy band compared with the traditional CdS [26–30]. Huang *et al.* [31] synthesized a CdZnS nanocrystalline solid solution with a controllable energy band and abundant sulfur vacancies by using a hydrothermal method. Chen *et al.* [32] synthesized CdZnS quantum dots with a controllable quantum size by using the template and ion-exchange methods and found that they exhibit excellent hydrogen evolution performance under visible light response. However, all metal sulfides suffer from photocorrosion, which severely limits the wide application of CdZnS photocatalysts. Heterostructures can effectively inhibit the photocorrosion and accelerate the separation of photogenerated carriers, thereby improving the PHE rate and stability of photocatalysts. Therefore, the rational design of N-C/CdZnS/In_2O_3 heterojunction photocatalysts is important to realize fast PHE.

[1] School of Physics and Technology, University of Jinan, Jinan 250022, China
[2] School of Electronic and Information Engineering (Department of Physics), Qilu University of Technology (Shandong Academy of Sciences), Jinan 250353, China
* Corresponding authors (emails: sps_xuxj@ujn.edu.cn (Xu X); sps_zhangsw@ujn.edu.cn (Zhang S))

In this work, hexagonal hollow tubular N-C/In_2O_3 is obtained through pyrolysis, and then CdZnS nanoparticles are uniformly attached to the surface of N-C/In_2O_3 by using a simple oil bath heating method to form a hierarchical heterostructure, as shown in Scheme 1. The optimized photocatalyst exhibits excellent PHE performance (~22.87 μmol h^{-1}), which is ~54.5 times that of pure In_2O_3 and better than those of previously reported In_2O_3-based photocatalytic materials. Therefore, this study provides novel ideas for developing renewable and clean energy under the current situation of limited reserves of traditional fossil energy.

EXPERIMENTAL SECTION

Materials and reagents

Cadmium acetate dihydrate ($Cd(CH_3COO)_2{\cdot}2H_2O$), indium nitrate hydrate ($In(NO_3)_3{\cdot}xH_2O$), 2-aminoterephthalic acid, and *N*,*N*-dimethylformamide (DMF) were purchased from Aladdin (Shanghai, China). Zinc acetate dihydrate ($Zn(CH_3COO)_2{\cdot}2H_2O$) and sodium sulfide nonahydrate ($Na_2S{\cdot}9H_2O$) were purchased from McLean (Shanghai, China). Triethanolamine (TEOA) and anhydrous ethanol were purchased from Sinopharm Chemical Reagent (Shanghai, China). All reagents were used as received, and deionized water (18 MΩ cm) was used in all experiments.

Synthesis of CdZnS nanoparticles

In brief, 0.5 mmol of $Zn(CH_3COO)_2{\cdot}2H_2O$ and 0.75 mol of $Cd(CH_3COO)_2{\cdot}2H_2O$ were dispersed in 60 mL of deionized water and stirred for 10 min. The mixture was added with 1.5 mmol of $Na_2S{\cdot}9H_2O$ and then placed in an oil bath at 80°C for 2 h. Finally, after cooling to room temperature, the yellow CdZnS product was collected by centrifugation, washed three times with deionized water, and then vacuum freeze-dried at −80°C. Similarly, orange-red CdS and white ZnS were synthesized following the same method except removing $Zn(CH_3COO)_2{\cdot}2H_2O$ and $Cd(CH_3COO)_2{\cdot}2H_2O$, respectively.

Synthesis of N-C/In_2O_3 and In_2O_3 hollow nanotubes

In brief, 2 mmol of $In(NO_3)_3{\cdot}xH_2O$ and 1.3 mmol of 2-aminoterephthalic acid were dispersed in 20 mL of DMF, sonicated for 10 min, and then vigorously stirred for 3 h. The solution was transferred to a 50-mL Teflon-lined autoclave and then stored at 125°C for 10 h. After cooling to room temperature, the solution was washed three times with anhydrous ethanol. The light yellow NH_2-MIL-68(In) sample was obtained by vacuum freeze drying at −80°C. It was placed into a magnetic boat, calcined in Ar atmosphere at 120°C for 2 h and then at 500°C for 2 h at a heating rate of 5°C min^{-1} to obtain black N-C/In_2O_3 hollow nanotubes. In the air atmosphere, NH_2-MIL-68(In) and $In(NO)_3$ were calcined in air at the same calcination temperature to obtain In_2O_3 and c-In_2O_3, respectively.

Synthesis of N-C/In_2O_3/CdZnS and In_2O_3/CdZnS

Typically, under vigorous stirring, an appropriate amount of N-C/In_2O_3 was dispersed in 60 mL of water and then sonicated for 15 min. The solution was added with 0.1 mmol of $Zn(CH_3COO)_2{\cdot}2H_2O$, 0.15 mmol of $Cd(CH_3COO)_2{\cdot}2H_2O$, and 0.3 mmol of $Na_2S{\cdot}9H_2O$ and then placed in an oil bath at 80°C for 2 h. After cooling to room temperature, the samples were collected by centrifugation, washed three times with deionized water to obtain light black samples, and then vacuum freeze-dried at −80°C. The sample was named "HTCZ-*x*," where *x* represents the mass of N-C/In_2O_3 added (*x* = 5, 10, 20, 30 mg). In_2O_3/CdZnS represents a composite formed by replacing N-C/In_2O_3 with In_2O_3 in the above reaction, wherein the mass of In_2O_3 was 20 mg.

Characterization

Powder X-ray diffraction (XRD) data were collected on an X-ray diffractometer (Hitani D/Ma-2500, Tokyo, Japan) using Cu Kα radiation. The scanning range was from 10° to 80°, and the scanning speed was 10° min^{-1}. X-ray photoelectron spectroscopy (XPS) was performed on an electron spectrometer (Thermo Fisher ESCALAB Xi+). Scanning electron microscopy (SEM) and transmission electron microscopy (TEM) were conducted using JSM-7500 and JEM-F200, respectively. The Raman spectra of the catalysts were obtained using Horiba LabRAM HR Evolution. Ultraviolet-visible (UV-Vis) diffuse reflectance spectroscopy (DRS) was performed on a Shimadzu UV-2600. UV-Vis spectrophotometer was based on barium sulfate. The specific surface area was calculated using the Brunauer-Emmett-Teller method. The N adsorption-desorption isotherms at −196°C were measured using an adsorption instrument (TriStarII, Micromeritics Company, USA) to evaluate the pore structure.

Photocatalytic H_2 evolution

The PHE experiments were carried out on a Perfect Light CEL-SPH2N system with a 300-W xenon lamp as the light source, and the temperature of the reaction vessel was controlled at 25 ± 0.5°C. The photocatalyst (10 mg) was added to the aqueous solution of TEOA (20 vol%) and then ultrasonically stirred for 30 min. Then, the solution was poured into a quartz reactor and evacuated with a vacuum pump. By using Ar as the carrier gas, the samples were analyzed every 30 min, and the amount of

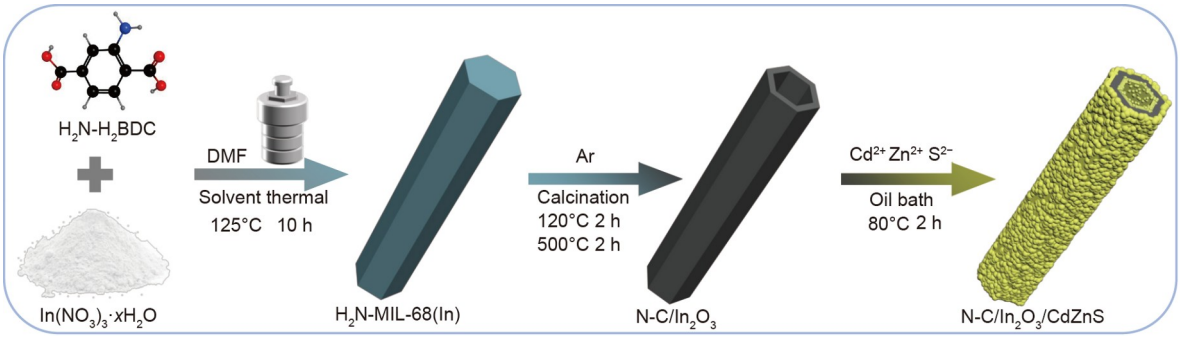

Scheme 1 Material preparation of N-C/In_2O_3/CdZnS.

hydrogen evolution was determined using online gas chromatography. The apparent quantum efficiency (AQE) was calculated as described in the Supplementary information.

Photoelectrochemical measurements

In an electrochemical workstation (Chenhua CHI760E, China), photoelectrochemical measurements were performed using a three-electrode system (Pt electrode, Ag/AgCl electrode, and working electrode) with 0.5 mol L^{-1} Na_2SO_4 as the electrolyte. The working electrode was prepared by adding 5 mg of photocatalyst to a mixed solution of 20 μL of Nafion and 2 mL of ethanol, ultrasonically treating it for 30 min, and then coating 100 μL of the suspension on fluorine-doped tin oxide (FTO) conductive glass. Transient photocurrents were collected under UV light irradiation at 365 nm. Electrochemical impedance spectroscopy (EIS) was performed at the frequency acquisition range of 0.01–10^6 Hz (bias potential is −0.2 V). The Mott-Schottky (M-S) test was conducted at the potential range of −1.0–1.0 V and frequencies of 0.5 and 1.0 kHz. The conversion between Ag/AgCl electrode potential and standard hydrogen electrode (NHE) potential was based on the Nernst equation:

$$E(vs.\ \text{NHE})=E(vs.\ \text{Ag/AgCl})+E_{\text{Ag/AgCl}}(\text{refer})+0.0591\text{pH},$$

$E_{\text{Ag/AgCl}}$(refer)=0.197 V *vs*. NHE at 25°C.

RESULTS AND DISCUSSION

Structure and morphology

XRD results show the successful synthesis of the hexagonal prism NH_2-MIL-68(In) with good crystallinity (Fig. 1a) [33–35]. N-C/In_2O_3 obtained by calcining NH_2-MIL-68(In) precursor under Ar has a typical cubic structure corresponding to standard cubic In_2O_3 (JCPDS No. 06-0416). Fig. 1a shows the crystal structure of the as-prepared CdZnS solid solution, whose diffraction peaks are located between those of cubic CdS (JCPDS No. 10-0454) and cubic ZnS (JCPDS No. 05-0566) [31]. The crystal structures of N-C/In_2O_3, CdZnS, and their composites in Fig. 1b exhibit diffraction peaks at 21.50°, 30.58°, 35.47°, 51.04°, and 60.68° in the composite, which correspond to the (211), (222), (400), (440), and (622) crystal planes of In_2O_3, respectively. In particular, the main characteristic peak at approximately 27.4° corresponds to the (111) crystal plane of CdZnS. Moreover, the intensities of diffraction peaks in the composites increase with increasing N-C/In_2O_3 mass, indicating the successful synthesis of N-C/In_2O_3/CdZnS heterostructure with high

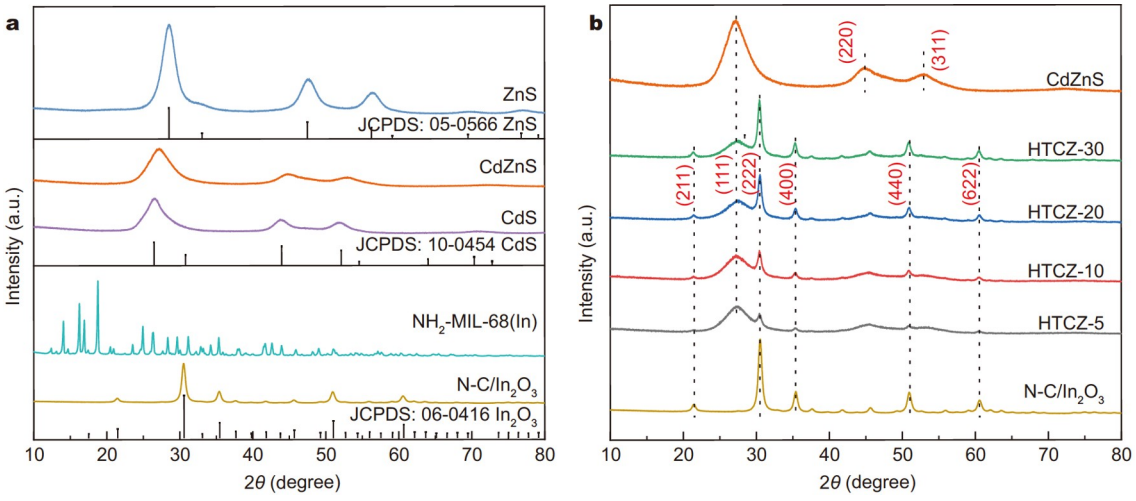

Figure 1 (a, b) XRD patterns of CdZnS, ZnS, CdS, NH_2-MIL-68(In), N-C/In_2O_3, and HTCZ-*x*.

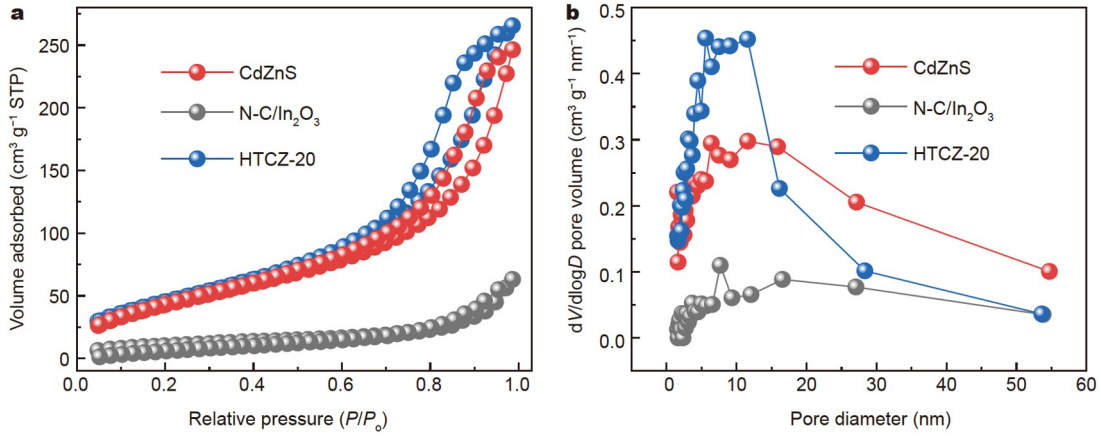

Figure 2 (a) N_2 adsorption-desorption isotherms and (b) pore size distributions of CdZnS, N-C/In_2O_3, and HTCZ-20.

crystallinity.

NH_2-MIL-68(In) in Fig. S1a, b shows that the solvothermally synthesized NH_2-MIL-68(In) exhibits a hexagonal prism shape with a smooth surface and a diameter of approximately 1–2 μm. In_2O_3 and N-C/In_2O_3 appear as hexagonal hollow tubes (Fig. S1c–f) that are slightly smaller than their precursors. CdZnS solid solutions composed of many fine nanoparticles are shown in Fig. S1g, h. TEM image of the N-C/In_2O_3 hexagonal hollow tubes is shown in Fig. S2a. The brighter contrast shows that the N-C/In_2O_3 surface is a mesoporous shell structure with a hollow interior, which is consistent with the SEM results. High-resolution TEM (HRTEM) image shows that its unique external porous structure is composed of 15–35 nm nanoparticles (Fig. S2b). This porous structure is generally believed to be due to the removal of organic ligands during the annealing [36,37]. This unique structural feature can provide more active sites for the photocatalytic reaction. The lattice spacings of 0.41 and 0.18 nm can be ascribed to the (211) and (521) planes of cubic In_2O_3, as shown in Fig. S2c. A thin amorphous carbon layer (1–2 nm) wrapped with In_2O_3 can be observed. The energy dispersive X-ray (EDX) spectrum shows that the concentration of C atoms reaches 37.2%, indicating that the carbon derived from organic ligands is maintained in the hollow structure and improves the stability of the hollow structure (Fig. S2d). The Raman spectrum of N-C/In_2O_3 shows two correlated carbon-related peaks at 1357 and 1575 cm^{-1} (Fig. S3a), which are derived from the D band of sp^3 carbon in disordered carbon and the G band of sp^2 carbon in graphite, respectively [38,39]. Pure In_2O_3 has no relevant peaks, indicating the existence of carbon-coated In_2O_3. The C 1s spectrum of N-C/In_2O_3 is shown in Fig. S3b. The peaks with binding energies of 284.80 and 288.80 eV correspond to C–C/C=C and C=O bonds, respectively [40], whereas the peak at 286.48 eV corresponds to C–N bonds, confirming the existence of a N-doped C layer [41,42]. The N 1s spectrum of N-C/In_2O_3 is shown in Fig. S3c. The peaks with binding energies of 399.55 and 398.10 eV are attributed to N_L lattice and N–C bonds, respectively, which further proves the existence of the N-doped carbon layer [43]. Scanning TEM (STEM) and its element mapping (Fig. S2e) also clearly present the uniform distribution of C, N, In, and O in N-C/In_2O_3. These detailed analyses prove that the N-doped C layer is coated on the hexagonal In_2O_3 hollow nanotubes.

As shown in Fig. S1i, j, the HTCZ-20 prepared in the oil bath still maintains the hexagonal hollow tube shape, suggesting its

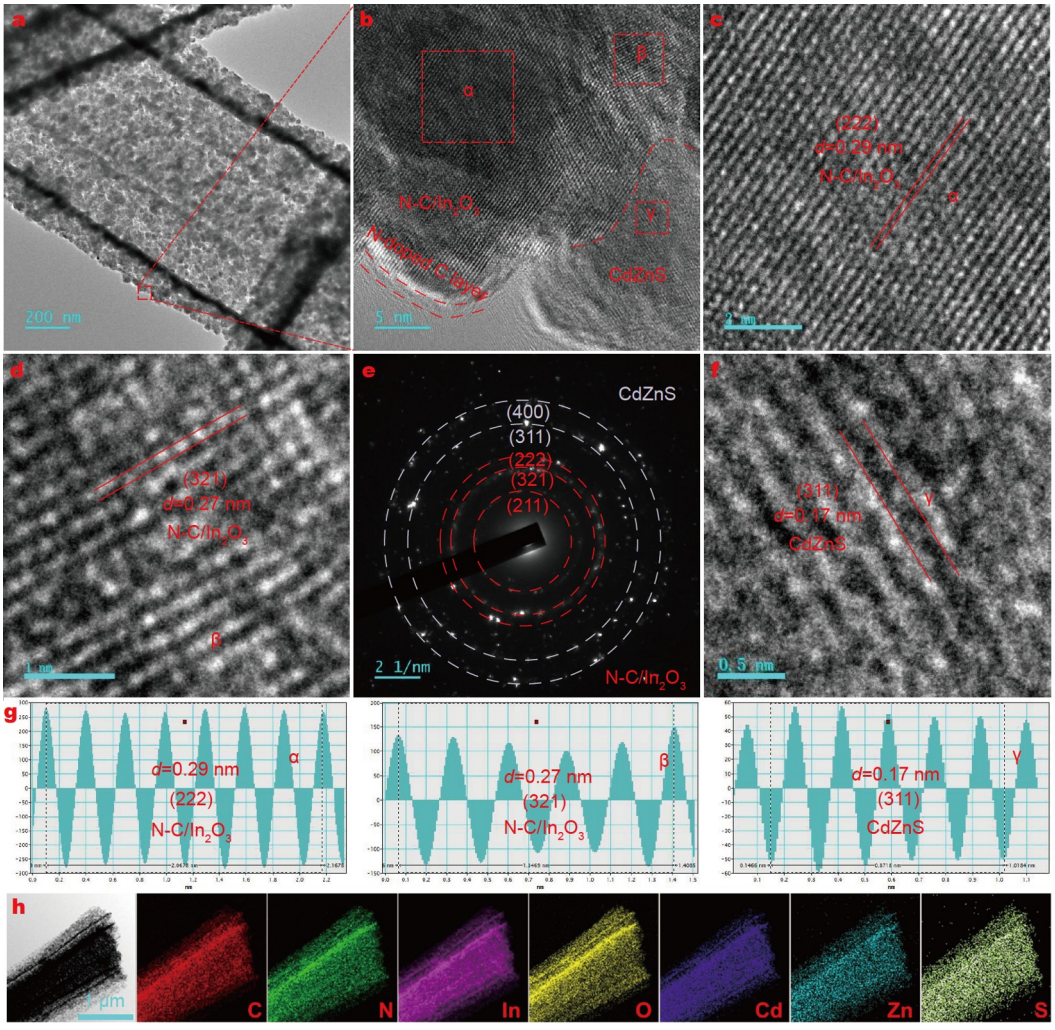

Figure 3 (a, b) TEM and HRTEM images of HTCZ-20; (c, d, f) enlarged HRTEM images form the marked area α, β, and γ in (b), respectively; (e) SAED patterns of HTCZ-20; (g) determined lattice spaces of N-C/In_2O_3 and CdZnS corresponding to α, β, and γ regions; (h) high-angle annular dark field (HAADF)-STEM image and corresponding element mappings of an individual HTCZ-20.

good structural stability. The surface of HTCZ-20 is rougher than that of N-C/In_2O_3 because of the decoration of CdZnS nanoparticles on the N-C/In_2O_3 surface. Meanwhile, the specific surface area and pore characteristics of the prepared samples in Fig. 2a, b show that CdZnS, HTCZ-20, and N-C/In_2O_3 exhibit IV type isotherms with H_3-type hysteresis loops, confirming the formation of mesopores (2–50 nm) from the loose packing of nanoparticles. The specific surface areas of CdZnS, HTCZ-20, and N-C/In_2O_3 are 167.61, 173.77, and 38.35 $m^2 g^{-1}$, respectively (Table S1). Compared with pure N-C/In_2O_3 and CdZnS, HTCZ-20 has a larger specific surface area, which is consistent with the SEM observations. The increased specific surface area and pore volume of the composites improve the surface contact with water molecules and expose more reactive sites, which promote the electron and mass transfer and ultimately improve the photocatalytic performance and hydrogen evolution rate [44].

The TEM image of HTCZ-20 in Fig. 3a exhibits its hollow tube structure, which is consistent with the SEM image (Fig. S1i, j). The lattice spacings of 0.29 and 0.27 nm can be attributed to the (222) and (321) planes of N-C/In_2O_3 (Fig. 3b–d), respectively, whereas the lattice spacing of 0.17 nm is ascribed to the (311) plane of CdZnS (Fig. 3f). The clear interface between N-C/In_2O_3 and CdZnS proves the heterojunction formation of the composites. Fig. 3b also shows that In_2O_3 is wrapped with a thin carbon layer, which is consistent with that shown in Fig. S2c. The corresponding selected area electron diffraction (SAED) patterns in Fig. 3e show two sets of diffraction rings, including the (222), (321) and (211) planes of cubic N-C/In_2O_3 and the (400) and (311) planes of CdZnS. The EDX spectrum (Fig. S4) and elemental mapping (Fig. 3h) confirm the uniform distribution of C, N, In, O, Cd, Zn, and S in HTCZ-20. These detailed analyses suggest the successful synthesis of N-doped, C-coated In_2O_3-CdZnS heterostructures with hexagonal hollow tubular shapes.

The XPS spectra of the chemical elemental states of CdZnS, N-C/In_2O_3, and HTCZ-20 are shown in Fig. S5. The HTCZ-20

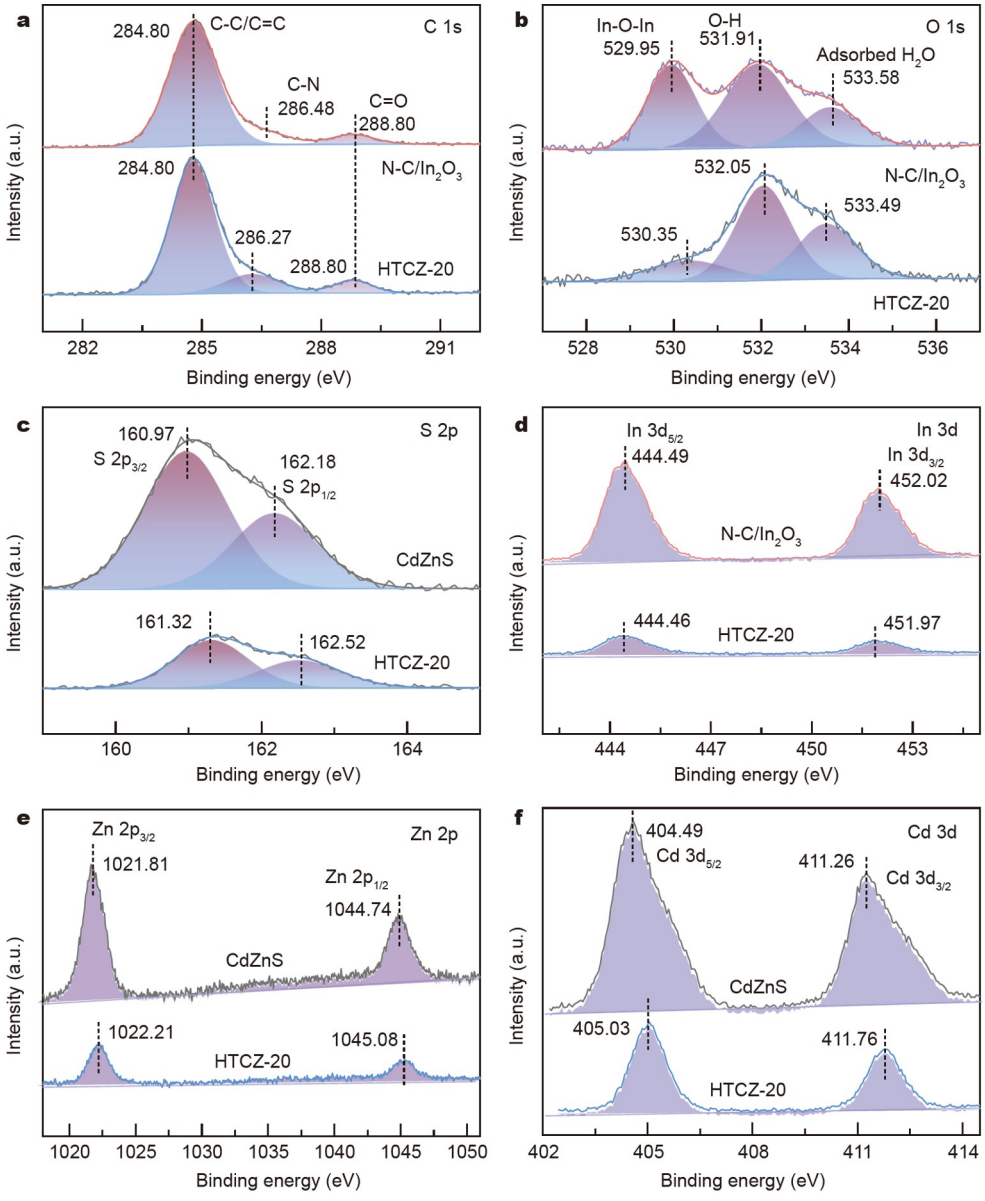

Figure 4 XPS spectra of N-C/In_2O_3, CdZnS, and HTCZ-20 samples: (a) C 1s, (b) O 1s, (c) S 2p, (d) In 3d, (e) Zn 2p, and (f) Cd 3d, respectively.

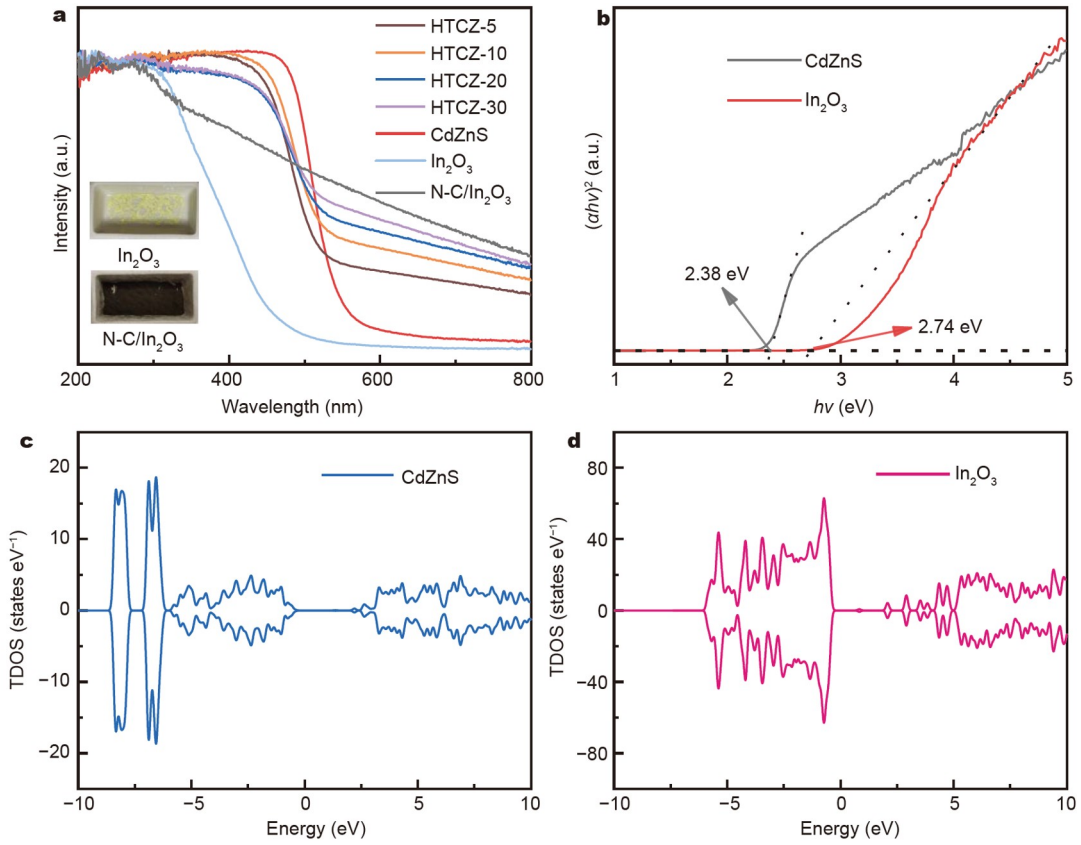

Figure 5 (a) UV-Vis DRS of In_2O_3, N-C/In_2O_3, CdZnS, and HTCZ-*x*; (b) corresponding Tauc plots of $(\alpha h\nu)^2$ *versus* $h\nu$ of In_2O_3 and CdZnS; (c, d) total density of states of CdZnS and In_2O_3.

sample has C, N, O, In, Cd, Zn, and S element signals, which are consistent with the element mapping (Fig. 3h). The C 1s spectrum of HTCZ-20 (Fig. 4a) can be deconvoluted into three peaks corresponding to the C–C/C=C (284.80 eV), C–N (286.27 eV), and C=O (288.80 eV) bonds. The O 1s spectrum of HTCZ-20 (Fig. 4b) is deconvoluted into three peaks at 530.35, 532.05, and 533.49 eV, which are attributed to In–O–In (O lattice), surface hydroxyl groups (O–H), and adsorbed water (H_2O), respectively [40,45]. The S 2p spectrum of HTCZ-20 (Fig. 4c) shows two peaks at 161.32 and 162.52 eV, which are assigned to S $2p_{3/2}$ and S $2p_{1/2}$, respectively [34,46]. Notably, the binding energies of the In $3d_{5/2}$ and In $3d_{3/2}$ peaks of the composite HTCZ-20 negatively shift (~0.05 eV) relative to N-C/In_2O_3, whereas the binding energies of the Zn 2p and Cd 3d peaks positively shift (~0.5 eV) relative to N-C/In_2O_3 (Fig. 4d–f). This phenomenon confirms the electronic coupling between N-C/In_2O_3 and CdZnS. Moreover, this negative binding energy shift means that the electron density on the In(III) site increases, and the positive binding energy shift means that the electron density on the Zn(II) and Cd(II) sites decreases [18]. Thus, CdZnS donates electrons to N-C/In_2O_3, and the heterojunction between CdZnS and N-C/In_2O_3 facilitates this electron transport, greatly accelerating the photocatalytic reaction rate. The XPS results indicate that the elements of the N-C/In_2O_3/CdZnS heterostructure present the chemical states of In^{3+}, Cd^{2+}, O^{2-}, Zn^{2+}, and S^{2-}, confirming the presence of CdZnS and In_2O_3 in the composite samples, which are consistent with the XRD and TEM results.

In PHE, the light absorption properties of photocatalysts greatly influence the photocatalytic activity. As shown in Fig. 5a, the light absorption performance of pure In_2O_3 is good in the UV light region but poor in the visible light region. N-C/In_2O_3 exhibits strong light absorption properties in the UV and visible light regions. This result can be attributed to the fact that the N-doped C layer makes In_2O_3 appear carbon black, which contributes to its excellent light absorption. Simultaneously, the N-C/In_2O_3 hollow tubular structure can cause multiple light reflections, which further enhance its light absorption [21,47]. As shown in Fig. S6, the light absorption properties of In_2O_3 with a hollow structure (Fig. S1c, d) and c-In_2O_3 with a non-hollow structure (Fig. S7) are similar, indicating that the N-doped C layer plays a major role in enhancing light absorption. For the HTCZ-20 heterostructures, a strong photoresponse can be found in the UV and visible light regions. With the increase in CdZnS loading, the absorption edge of HTCZ has an obvious red shift, indicating its enhanced visible light response. Furthermore, the band gaps of In_2O_3 and CdZnS are calculated using the Kubelka-Munk function $\alpha h\nu = A(h\nu - E_g)^{n/2}$ [48]. As In_2O_3 and CdZnS are both indirect-band-gap semiconductors (n = 4), their band gaps are calculated to be 2.74 and 2.38 eV, respectively (Fig. 5b). Meanwhile, the total densities of states (TDOS) of CdZnS and In_2O_3 are calculated using the density functional theory (DFT). The theoretical E_g values of CdZnS and In_2O_3 are similar to the experimental values (Fig. 5c, d).

PHE performance

The PHE rate of pristine CdZnS nanoparticles is ~9.49 μmol h^{-1}, whereas N-C/In_2O_3 (0 μmol h^{-1}) and In_2O_3 (~0.42 μmol h^{-1}) show almost no photocatalytic activities (Fig. 6a, b). After

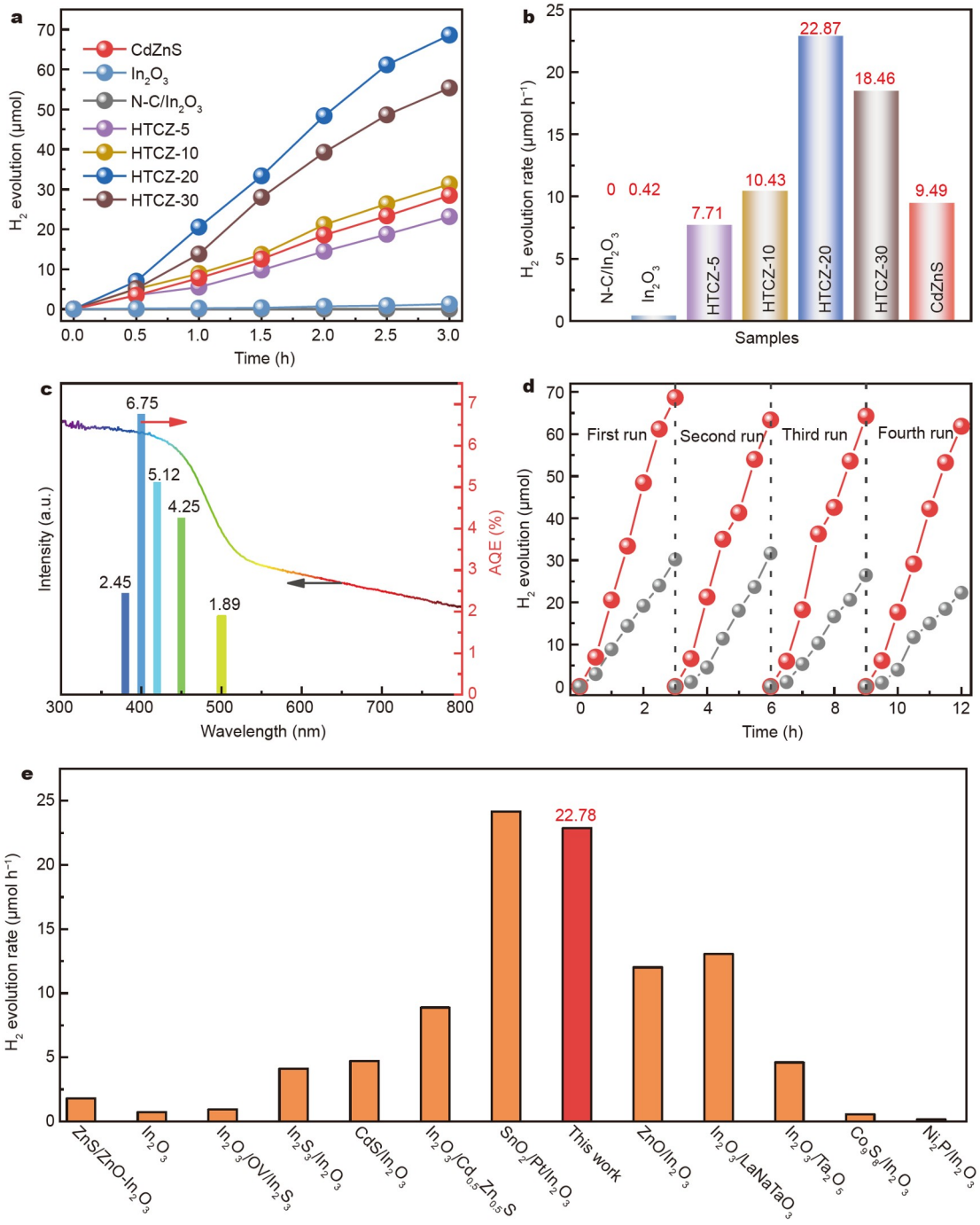

Figure 6 (a) Photocatalytic H_2 evolution performances and (b) evolution rates of different photocatalysts; (c) UV-Vis DRS of HTCZ-20 and AQE of PHE with monochromatic light irradiation; (d) cycling H_2 evolution curves of HTCZ-20 and CdZnS; (e) PHE rate of HTCZ-20 is compared with those of typical In_2O_3 or CdZnS-based photocatalysts reported previously.

assembly with CdZnS nanoparticles, HTCZ-20 exhibits the highest photocatalytic rate (~22.87 μmol h^{-1}), which is approximately 54.5 times that of pure In_2O_3, whereas HTCZ-5 exhibits a lower photocatalytic rate (~7.71 μmol h^{-1}), approximately 18.4 times that of pure In_2O_3. These results indicate that the mass ratio of the components affects the photocatalytic performance, and the assembly of excessive or insufficient CdZnS nanoparticles influences the PHE rate. A comparison of the PHE rates of HTCZ-20, In_2O_3/CdZnS (~17.46 μmol h^{-1}), CdS (~6.88 μmol h^{-1}), and ZnS (0 μmol h^{-1}) is shown in Fig. S8. The PHE rate of HTCZ-20 is larger than those of the others, showing that the N-doped C layer between CdZnS and In_2O_3 accelerates the photocatalytic reaction rate. The AQEs of HTCZ-20 at various wavelengths in Fig. 6c show that AQE and incident wavelength are almost positively correlated with the highest value of 6.75% at 400 nm. Therefore, the stronger the photoresponse of the photocatalyst, the more excited photogenerated carriers are, and the more the photocatalytic rate can be

improved. These findings further prove that the high hydrogen evolution rate of HTCZ-20 is due to the strong light absorption properties of N-C/In_2O_3. The cycling stabilities of HCTZ-20 and CdZnS were tested after four cycles. HTCZ-20 can still maintain more than 90% of the original PHE rate, whereas CdZnS can only maintain more than 70% of the original PHE rate (Fig. 6d).

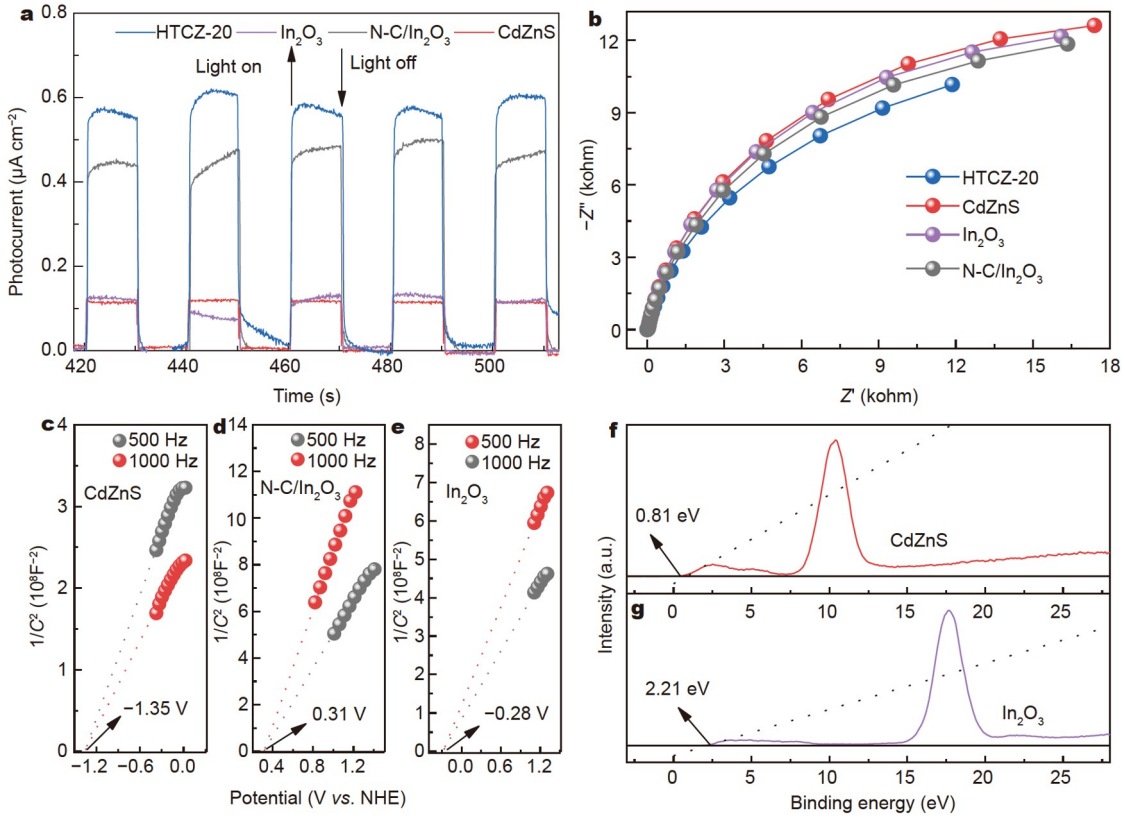

Figure 7 (a) Transient photocurrent responses and (b) EIS spectra of In_2O_3, N-C/In_2O_3, CdZnS, and HTCZ-20; M-S plots of (c) CdZnS, (d) N-C/In_2O_3, and (e) In_2O_3; VB-XPS spectra of (f) CdZnS and (g) In_2O_3.

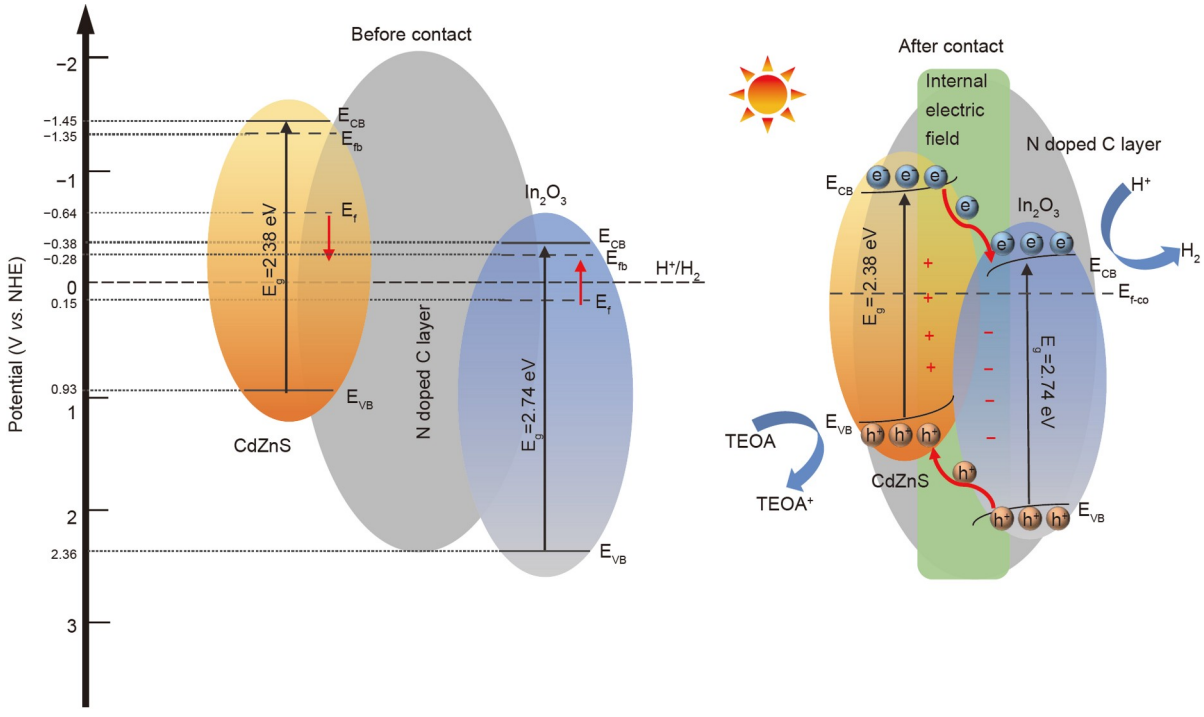

Figure 8 Reaction mechanism of HTCZ-20 photocatalyst.

As shown in Fig. S9, the SEM image and XRD pattern of HTCZ-20 show that the morphology and structure of HTCZ-20 remain unchanged after four cycles of testing. This result indicates that the HTCZ-20 heterostructure has high cycling stability. In addition, the effects of different sacrificial agents on PHE were investigated. Results show that the weak alkaline aqueous solution has better PHE effect than the weak acid solution, and Na_2S/Na_2SO_3 can be considered instead of TEOA, and their PHE effects are similar (Fig. S10a). The effect of photocatalyst dosage on PHE is shown in Fig. S10b. When the photocatalyst is larger than 10 mg, the amount of PHE does not increase significantly because the excess photocatalyst affects the light absorption and reduces the photocatalytic activity. As shown in Fig. S11, the amount of PHE of HTCZ-20 is much higher than that of mechanically mixed samples, indicating that the core-shell structure of the HTCZ-20 photocatalyst is conducive to the photocatalytic reaction, which further proves the formation of HTCZ-20 heterostructure. Moreover, comparisons with other In_2O_3-based and CdZnS-based photocatalysts show that the hydrogen evolution rate of HTCZ-20 is superior to those of previously reported photocatalysts and comparable to that of SnO_2/Pt/In_2O_3 with Pt cocatalysts (Fig. 6e and Table S2).

Photocatalytic mechanism

Transient photocurrent spectroscopy and EIS were used to analyze the transfer and separation capabilities of photogenerated carriers. In_2O_3 (~0.13 μA cm^{-2}) and CdZnS (~0.12 μA cm^{-2}) show lower photocurrent responses, whereas N-C/In_2O_3 (~0.45 μA cm^{-2}) and HTCZ-20 (~0.58 μA cm^{-2}) exhibit higher photocurrent responses than In_2O_3 and CdZnS (Fig. 7a). This result indicates that the formation of highly conductive N-C layers and the construction of heterostructures accelerate the separation and transfer of photogenerated carriers. In addition, HTCZ-20 (Fig. 7b) has the smallest semicircle in Nyquist plots among the photogenerated carriers, and N-C/In_2O_3 has a smaller semicircle than In_2O_3. These results further demonstrate that the photogenerated carriers are well transferred and separated at the N-C layer and the interface of the In_2O_3-CdZnS heterojunction.

Further, the M-S spectra and XPS valence band spectra were tested to determine the energy band structure and Fermi level (E_f) position of the photocatalysts. As shown in Fig. 7c–e, CdZnS, N-C/In_2O_3, and In_2O_3 all show positive slopes, indicating typical n-type semiconductor properties. The M-S diagram shows that the flat band potentials (E_{fb}) of CdZnS, N-C/In_2O_3, and In_2O_3 are −1.35, 0.31, and −0.28 V, respectively (*vs.* NHE). In general, the conduction band (E_{CB}) of 0.1–0.3 V is more negative than E_f, which is 0.1 V [49,50]. Therefore, the E_{CB} potentials of CdZnS, N-C/In_2O_3, and In_2O_3 are −1.45, 0.21, and −0.38 V, respectively. The E_{CB} potential (0.21 V) of N-C/In_2O_3 is higher than that of H^+/H_2 (0 V *vs.* NHE), whereas that of In_2O_3 (−0.38 V) is lower than that of H^+/H_2. Therefore, In_2O_3 can photocatalyze hydrogen production, whereas N-C/In_2O_3 cannot, which is consistent with the PHE results (Fig. 6b). The valence bands (E_{VB}) of CdZnS and In_2O_3 were calculated using the Kubelka-Munk formula ($E_g = E_{VB} - E_{CB}$) to be 0.93 and 2.36 V, respectively. As shown in Fig. 7f, g, the VB-XPS images show that the gaps between the top of the E_{VB} band of CdZnS and In_2O_3 to the E_f are 0.81 and 2.21 eV, respectively. Therefore, based on the E_{VB} positions, the E_f positions of CdZnS and In_2O_3 can be determined to be −0.64 and 0.15 V, respectively. The detailed band structures and E_f of pristine CdZnS and In_2O_3 are shown in Fig. 8 (before contact). In terms of theoretical simulation, the three-dimensional charge density difference is shown in Fig. 9a. The results show that electrons migrate from CdZnS to In_2O_3; CdZnS near the interface is positively charged, and In_2O_3 is negatively charged. Therefore, DFT calculation results indicate that a heterostructure is formed between CdZnS and In_2O_3, and the electron transfer direction is CdZnS to In_2O_3.

As part of their photocatalytic mechanism, CdZnS and In_2O_3, given their different E_f positions, are both close to their conduction band positions. When CdZnS is in contact with In_2O_3, the E_f of CdZnS will move down and the E_f of In_2O_3 will move up. Concurrently, a built-in electric field is formed at the heterojunction interface between CdZnS and In_2O_3, which eventually leads to the upward and downward bending of the CdZnS and In_2O_3 energy bands, respectively. The above analyses, combined with the DFT calculation results (Fig. 9a), confirm that the HTCZ-20 composite forms a type-II heterostructure, as shown in Fig. 8 (after contact). Under visible light irradiation, photogenerated electrons transfer from the E_{CB} of CdZnS to the E_{CB} of In_2O_3, and the holes transfer from the E_{VB} of In_2O_3 to the

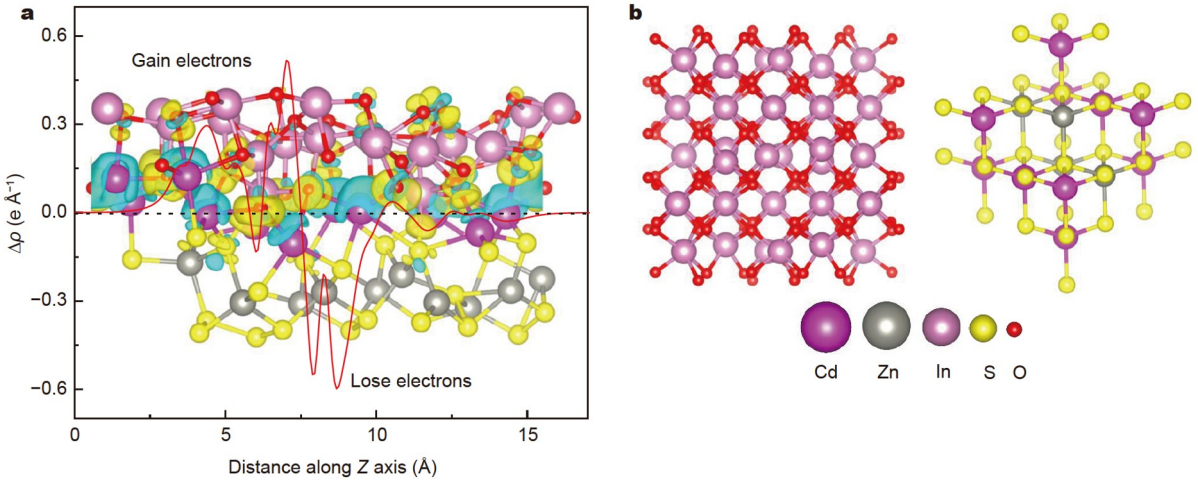

Figure 9 (a) Planar averaged electron density difference $\Delta\rho(z)$ along the Z direction for CdZnS-In_2O_3 heterostructure (blue and yellow areas indicate the loss and accumulation of electrons, respectively), (b) crystal structures of In_2O_3 and CdZnS.

E_{VB} of CdZnS. The N-C layer of N-C/In_2O_3 mainly serves as a bridge for the charge transfer between In_2O_3 and CdZnS. Finally, the photogenerated electrons accumulated in the E_{CB} of In_2O_3 reduce H^+ in water to form H_2, and the holes accumulated in the E_{VB} of CdZnS are captured by the sacrificial agent. In conclusion, n-n-type heterojunction semiconductor photocatalysts can improve the separation of photogenerated electrons and holes without impairing their redox ability through the accelerated drift of a built-in electric field.

CONCLUSION

In summary, hexagonal hollow tubular N-C/In_2O_3/CdZnS heterojunction photocatalysts were successfully synthesized. Under visible light irradiation, N-C/In_2O_3/CdZnS exhibits an excellent PHE rate (22.87 μmol h^{-1}) and good stability (four cycles, more than 90% photocatalytic efficiency). The excellent photocatalytic performance of N-C/In_2O_3/CdZnS is mainly attributed to the synergistic effect of its n-n-type heterostructure and the N-C layer acting as an electron transport bridge. This study provides a novel idea for developing efficient and stable photocatalysts.

Received 6 June 2022; accepted 26 July 2022; published online 21 October 2022

1 Wang Q, Domen K. Particulate photocatalysts for light-driven water splitting: Mechanisms, challenges, and design strategies. Chem Rev, 2020, 120: 919–985
2 Qi MY, Conte M, Anpo M, *et al.* Cooperative coupling of oxidative organic synthesis and hydrogen production over semiconductor-based photocatalysts. Chem Rev, 2021, 121: 13051–13085
3 Feng L, Pang J, She P, *et al.* Metal-organic frameworks based on group 3 and 4 metals. Adv Mater, 2020, 32: 2004414
4 Xia B, Zhang Y, Shi B, *et al.* Photocatalysts for hydrogen evolution coupled with production of value-added chemicals. Small Methods, 2020, 4: 2000063
5 Zuo Q, Liu T, Chen C, *et al.* Ultrathin metal-organic framework nanosheets with ultrahigh loading of single Pt atoms for efficient visible-light-driven photocatalytic H_2 evolution. Angew Chem Int Ed, 2019, 58: 10198–10203
6 Hou J, Cao S, Sun Y, *et al.* Atomically thin mesoporous In_2O_{3-x}/In_2S_3 lateral heterostructures enabling robust broadband-light photo-electrochemical water splitting. Adv Energy Mater, 2018, 8: 1701114
7 Tan M, Ma Y, Yu C, *et al.* Boosting photocatalytic hydrogen production *via* interfacial engineering on 2D ultrathin Z-scheme $ZnIn_2S_4$/g-C_3N_4 heterojunction. Adv Funct Mater, 2022, 32: 2111740
8 Khan K, Tao X, Shi M, *et al.* Visible-light-driven photocatalytic hydrogen production on $Cd_{0.5}Zn_{0.5}S$ nanorods with an apparent quantum efficiency exceeding 80%. Adv Funct Mater, 2020, 30: 2003731
9 Zhang W, Zhou X, Huang J, *et al.* Noble metal-free core-shell CdS/iron phthalocyanine Z-scheme photocatalyst for enhancing photocatalytic hydrogen evolution. J Mater Sci Tech, 2022, 115: 199–207
10 Zhang W, Zhao S, Xing Y, *et al.* Sandwich-like P-doped h-BN/$ZnIn_2S_4$ nanocomposite with direct Z-scheme heterojunction for efficient photocatalytic H_2 and H_2O_2 evolution. Chem Eng J, 2022, 442: 136151
11 Li W, Wang X, Ma Q, *et al.* CdS@h-BN heterointerface construction on reduced graphene oxide nanosheets for hydrogen production. Appl Catal B-Environ, 2021, 284: 119688
12 Zhan X, Zheng Y, Li B, *et al.* Rationally designed $Ta_3N_5/ZnIn_2S_4$ 1D/2D heterojunctions for boosting visible-light-driven hydrogen evolution. Chem Eng J, 2022, 431: 134053
13 Hou H, Shao G, Yang W. Recent advances in g-C_3N_4-based photocatalysts incorporated by MXenes and their derivatives. J Mater Chem A, 2021, 9: 13722–13745
14 Wang Q, Astruc D. State of the art and prospects in metal-organic framework (MOF)-based and MOF-derived nanocatalysis. Chem Rev, 2020, 120: 1438–1511
15 Nguyen HL. Metal-organic frameworks can photocatalytically split water—Why not? Adv Mater, 2022, 34: 2200465
16 Liu J, Feng J, Lu L, *et al.* A metal-organic-framework-derived $(Zn_{0.95}Cu_{0.05})_{0.6}Cd_{0.4}S$ solid solution as efficient photocatalyst for hydrogen evolution reaction. ACS Appl Mater Interfaces, 2020, 12: 10261–10267
17 Song Y, Li Z, Zhu Y, *et al.* Titanium hydroxide secondary building units in metal-organic frameworks catalyze hydrogen evolution under visible light. J Am Chem Soc, 2019, 141: 12219–12223
18 Yang H, Tang J, Luo Y, *et al.* MOFs-derived fusiform In_2O_3 mesoporous nanorods anchored with ultrafine CdZnS nanoparticles for boosting visible-light photocatalytic hydrogen evolution. Small, 2021, 17: 2102307
19 Shen Q, Zhou S, Yang FL, *et al.* Engineering one-dimensional hollow beta-In_2S_3/In_2O_3 hexagonal micro-tubes for efficient broadband-light photocatalytic performance. J Mater Chem A, 2022, 10: 4974–4980
20 Han L, Jing F, zhang J, *et al.* Environment friendly and remarkably efficient photocatalytic hydrogen evolution based on metal organic framework derived hexagonal/cubic In_2O_3 phase-junction. Appl Catal B-Environ, 2021, 282: 119602
21 Li R, Sun L, Zhan W, *et al.* Engineering an effective noble-metal-free photocatalyst for hydrogen evolution: Hollow hexagonal porous microrods assembled from In_2O_3@carbon core-shell nanoparticles. J Mater Chem A, 2018, 6: 15747–15754
22 Zhou X, Luo J, Jin B, *et al.* Sustainable synthesis of low-cost nitrogen-doped-carbon coated Co_3W_3C@g-C_3N_4 composite photocatalyst for efficient hydrogen evolution. Chem Eng J, 2021, 426: 131208
23 Wang A, Chen Y, Zheng Z, *et al. In situ* N-doped carbon-coated mulberry-like cobalt manganese oxide boosting for visible light driving photocatalytic degradation of pharmaceutical pollutants. Chem Eng J, 2021, 411: 128497
24 Yang W, Ma G, Fu Y, *et al.* Rationally designed Ti_3C_2 MXene@TiO_2/$CuInS_2$ Schottky/S-scheme integrated heterojunction for enhanced photocatalytic hydrogen evolution. Chem Eng J, 2022, 429: 132381
25 Zhan X, Fang Z, Li B, *et al.* Rationally designed Ta_3N_5@ReS_2 heterojunctions for promoted photocatalytic hydrogen production. J Mater Chem A, 2021, 9: 27084–27094
26 Lin S, Li S, Huang H, *et al.* Synergetic piezo-photocatalytic hydrogen evolution on $Cd_xZn_{1-x}S$ solid-solution 1D nanorods. Small, 2022, 18: 2106420
27 Lin S, Zhang Y, You Y, *et al.* Bifunctional hydrogen production and storage on 0D-1D heterojunction of $Cd_{0.5}Zn_{0.5}S$@halloysites. Adv Funct Mater, 2019, 29: 1903825
28 Kai S, Xi B, Wang Y, *et al.* One-pot synthesis of size-controllable core-shell CdS and derived CdS@$Zn_xCd_{1-x}S$ structures for photocatalytic hydrogen production. Chem Eur J, 2017, 23: 16653–16659
29 Zhong T, Yu Z, Jiang R, *et al.* Surface-activated $Ti_3C_2T_x$ MXene co-catalyst assembled with CdZnS-formed 0D/2D CdZnS/Ti_3C_2-A_{40} Schottky heterojunction for enhanced photocatalytic hydrogen evolution. Sol RRL, 2022, 6: 2100863
30 Ha E, Ruan S, Li D, *et al.* Surface disorder engineering in ZnCdS for cocatalyst free visible light driven hydrogen production. Nano Res, 2022, 15: 996–1002
31 Huang HB, Fang ZB, Yu K, *et al.* Visible-light-driven photocatalytic H_2 evolution over CdZnS nanocrystal solid solutions: Interplay of twin structures, sulfur vacancies and sacrificial agents. J Mater Chem A, 2020, 8: 3882–3891
32 Chen J, Lv S, Shen Z, *et al.* Novel ZnCdS quantum dots engineering for enhanced visible-light-driven hydrogen evolution. ACS Sustain Chem Eng, 2019, 7: 13805–13814
33 Liang R, Shen L, Jing F, *et al.* NH_2-mediated indium metal-organic framework as a novel visible-light-driven photocatalyst for reduction of the aqueous Cr(VI). Appl Catal B-Environ, 2015, 162: 245–251
34 Hou Q, Li X, Pi Y, *et al.* Construction of In_2S_3@NH_2-MIL-68(In)@In_2S_3 sandwich homologous heterojunction for efficient CO_2 photoreduction. Ind Eng Chem Res, 2020, 59: 20711–20718
35 Zhang Q, Gu H, Wang X, *et al.* Robust hollow tubular $ZnIn_2S_4$ modified with embedded metal-organic-framework-layers: Extraordinarily high photocatalytic hydrogen evolution activity under simulated and real sunlight irradiation. Appl Catal B-Environ, 2021, 298: 120632

36 Zhang X, Zhang S, Tang Y, *et al.* Recent advances and challenges of metal-organic framework/graphene-based composites. Compos Part B-Eng, 2022, 230: 109532
37 Pan T, Shen Y, Wu P, *et al.* Thermal shrinkage behavior of metal-organic frameworks. Adv Funct Mater, 2020, 30: 2001389
38 Li F, Liu Y, Mao B, *et al.* Carbon-dots-mediated highly efficient hole transfer in I–III–VI quantum dots for photocatalytic hydrogen production. Appl Catal B-Environ, 2021, 292: 120154
39 Wang Y, Liu X, Liu J, *et al.* Carbon quantum dot implanted graphite carbon nitride nanotubes: Excellent charge separation and enhanced photocatalytic hydrogen evolution. Angew Chem Int Ed, 2018, 57: 5765–5771
40 Wang S, Guan BY, Lou XWD. Construction of $ZnIn_2S_4$-In_2O_3 hierarchical tubular heterostructures for efficient CO_2 photoreduction. J Am Chem Soc, 2018, 140: 5037–5040
41 Sun L, Zhuang Y, Yuan Y, *et al.* Nitrogen-doped carbon-coated CuO-In_2O_3 p-n heterojunction for remarkable photocatalytic hydrogen evolution. Adv Energy Mater, 2019, 9: 1902839
42 Zhang Q, Zhang J, Wang X, *et al.* In-N-In sites boosting interfacial charge transfer in carbon-coated hollow tubular In_2O_3/$ZnIn_2S_4$ heterostructure derived from In-MOF for enhanced photocatalytic hydrogen evolution. ACS Catal, 2021, 11: 6276–6289
43 Sun L, Li R, Zhan W, *et al.* Rationally designed double-shell dodecahedral microreactors with efficient photoelectron transfer: N-doped-C-encapsulated ultrafine In_2O_3 nanoparticles. Chem Eur J, 2019, 25: 3053–3060
44 Fang LJ, Li YH, Liu PF, *et al.* Facile fabrication of large-aspect-ratio g-C_3N_4 nanosheets for enhanced photocatalytic hydrogen evolution. ACS Sustain Chem Eng, 2017, 5: 2039–2043
45 Zhao S, Li K, Wu J, *et al.* Metal-organic framework-derived tubular In_2O_3-C/$CdIn_2S_4$ heterojunction for efficient solar-driven CO_2 conversion. ACS Appl Mater Interfaces, 2021, 14: 20375–20384
46 Huang L, Li B, Su B, *et al.* Fabrication of hierarchical Co_3O_4@$CdIn_2S_4$ p-n heterojunction photocatalysts for improved CO_2 reduction with visible light. J Mater Chem A, 2020, 8: 7177–7183
47 Wang Q, Chen Y, Liu X, *et al.* Sulfur doped In_2O_3-CeO_2 hollow hexagonal prisms with carbon coating for efficient photocatalytic CO_2 reduction. Chem Eng J, 2021, 421: 129968
48 Cao R, Yang H, Zhang S, *et al.* Engineering of Z-scheme 2D/3D architectures with $Ni(OH)_2$ on 3D porous g-C_3N_4 for efficiently photocatalytic H_2 evolution. Appl Catal B-Environ, 2019, 258: 117997
49 Ouyang C, Quan X, Zhang C, *et al.* Direct Z-scheme $ZnIn_2S_4$@MoO_3 heterojunction for efficient photodegradation of tetracycline hydrochloride under visible light irradiation. Chem Eng J, 2021, 424: 130510
50 Yang YY, Zhang XG, Niu CG, *et al.* Dual-channel charges transfer strategy with synergistic effect of Z-scheme heterojunction and LSPR effect for enhanced quasi-full-spectrum photocatalytic bacterial inactivation: New insight into interfacial charge transfer and molecular oxygen activation. Appl Catal B-Environ, 2020, 264: 118465

Acknowledgements This work was supported by the Independent Cultivation Program of Innovation Team of Jinan City (2019GXRC011), the Natural Science Foundation of Shandong Province (ZR2021ME143), and the National Natural Science Foundation of China (51908242).

Author contributions Zhang W conducted the experiment and wrote the paper; Zhao S carried out theoretical calculations; Qin H, Zheng Q and Zhang P analyzed the data; Li X and Li C drew the graphs; Wang T and Li N validated the experiment; Xu X provided financial support and useful suggestions; Zhang S put forward useful suggestions.

Conflict of interest The authors declare that they have no conflict of interest.

Supplementary information Supporting data are available in the online version of the paper.

Weijie Zhang received a bachelor degree from the School of Physical Science and Technology at the University of Jinan in 2020. He is now pursing his master degree under the supervision of Prof. Xijin Xu at the School of Physics and Technology, University of Jinan, China. His main research interest is the synthesis and characterization of two-dimensional nanomaterials for photocatalytic applications.

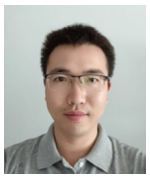

Shouwei Zhang received his PhD from Hefei University of Technology in 2015. His main interest is the preparation of photocatalytic materials.

Xijin Xu received his PhD degree from the Institute of Solid State Physics, Chinese Academy of Sciences in 2007. He conducted his postdoctoral research at Nanyang Technological University, Singapore in 2007 and then joined the National Institute for Materials Science, Japan (2008–2010) and Griffith University in Australia (2010–2011). Currently, he is a full professor at the University of Jinan. His most recent research interests include the synthesis and characterization of functional micro/nanostructures and their applications in environmental remediation and energy storage.

金属有机框架衍生的氮掺杂碳包覆空心管In_2O_3/CdZnS异质结用于高效光催化析氢

张伟杰[1], 赵顺顺[2], 秦鸿杰[1], 郑其玲[1], 张鹏辉[1], 李晓娟[1], 李传琳[1], 王同凯[1], 李娜[1], 张守伟[1*], 徐锡金[1*]

摘要 光催化析氢(PHE)技术是解决当前能源短缺问题的有力途径之一. 本文采用简单的油浴加热方法原位合成了六方空心管状氮掺杂碳包覆的In_2O_3/CdZnS异质结光催化剂. 结果表明, N-C/In_2O_3/CdZnS (~22.87 μmol h^{-1})的光催化析氢速率是原始CdZnS (~9.49 μmol h^{-1})的~2.4倍, 是原始In_2O_3(~0.42μmol h^{-1})的~54.5倍. 经过4个循环后, 光催化析氢量仍能达到原来的90%以上. 其优异的光催化性能主要归功于以下几个方面: (1) 氮掺杂碳层作为电子传输桥梁, 保证了光催化反应的高效电子转移; (2) 中空管状结构增强了光的反射, 增强了光吸收性能; (3) 形成N-C/In_2O_3/CdZnS异质结构, 改善了载流子复合和光腐蚀问题; (4) 大的比表面积和介孔结构提供了大量的反应位点. 因此, 本研究为设计可见光型异质结催化剂提供了新思路.

